RSC Advances

ROYAL SOCIETY OF CHEMISTRY

www.rsc.org/advances

Table of contents entry

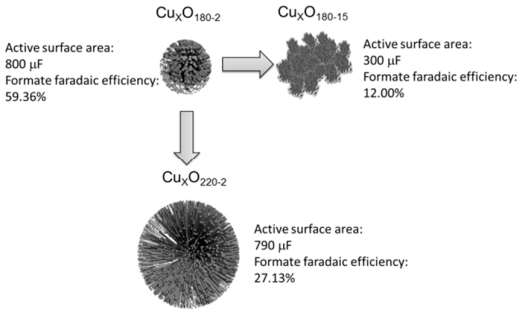

The Cu_XO_{180-2} catalyst obtained with 3D hierarchical nanosphere structures could catalyze CO_2 reduction in aqueous solution with very high catalytic activity and superb selectivity of produced formate, significantly outperforming Cu_XO catalysts without such special morphology.

Revised version: RA-ART-08-2014-009442R3

Aqueous CO_2 reduction on morphology controlled Cu_XO nanocatalysts at low overpotential

Mengyang Fan[a], Zhengyu Bai[b], Qing Zhang[b], Chenyu Ma[a,c*]

Xiaodong Zhou[d*], Jinli Qiao[a,b*]

[a]*College of Environmental Science and Engineering, Donghua University, 2999 Ren'min North Road, Shanghai 201620, P. R. China*

[b]*School of Chemistry and Chemical Engineering, Key Laboratory of Green Chemical Media and Reactions, Ministry of Education, Henan Normal University, Xinxiang, Henan 453007, P. R. China*

[c]*Department of Chemistry and Environmental Science, Kashigar Teachers College, Kashgar, 844006, P. R. Chin*

[d]*Department of Chemical Engineering, University of South Carolina, Columbia, SC 29208*

Corresponding author. Tel: +81-90-6008-9342, +86-21-67792379. Fax: +86-21-67792159. E-mail: qiaojl@dhu.edu.cn, machengyu@dhu.edu.cn , zhox@cec.sc.edu

Aqueous CO_2 reduction on morphology controlled Cu_XO nanocatalysts at low overpotential

Mengyang Fan, Zhengyu Bai, Qing Zhang, Chenyu Ma, Xiaodong Zhou, Jinli Qiao

Abstract: Various Cu_XO catalysts with different special microstructures were synthesized using a simple one-step hydrothermal method by controlling the reaction time and temperature conditions. Scanning electron microscopy (SEM) and high-resolution transmission electron microscopy (HR-TEM) was used to observe the morphologies of received catalysts. The 3-dimension (3D) hierarchical nanospheres (500 nm) comprised of secondary structured nanorods (50 nm) are formed at 180^{o}C for 2 hours. However, when increasing the hydrothermal reaction temperature to 220^{o}C, solid microspheres with large size of 2.5 μm begin to appear instead of flabby hierarchical nanospheres. To further investigate the effect of morphologies on the activity and production selectivity of Cu_XO catalysts, cyclic voltammetry (CV) was used to evaluate the onset potential and current density of catalyzed CO_2 reduction combing linear sweep voltammetry (LSV) in 0.5 M $KHCO_3$ solution. The effect of catalyst loading was also tested by applying the gas diffusion layer (GDL) to make up a working electrode for CO_2 electroreduction. The results indicate that the synthesized temperature at 180^{o}C for 2h is the optimal condition for Cu_XO nanospheres and, the optimal loading is about 3 mg cm^{-2}, under which the onset potential for CO_2 electroreduction reaches -0.55 V vs. SHE. By ion chromatography measurement, the Faradaic efficiency and production rate of produced formate was found to be 59%, which is much higher than most reported Cu-based catalysts at the same electrolysis conditions, indicating the high selectivity of the Cu_XO nanospheres due to its controlled special surface morphology.

Keywords: CO_2 electroreduction, copper oxide nanoscatalysts, morphology control, secondary structure, formate production, selectivity

1. Introduction

Extra emission of carbon dioxide (CO_2) into the atmosphere, induced by the depletion of non-renewable fossil fuels and excess human industrial activities, has been considered one of the primary causes in possible global warming due to the greenhouse effect, and also becoming an increasing concern in recent years. Electrochemical reduction of CO_2 to form useful chemicals or fuels is a potentially efficient method of CO_2 utilization and recycling.[1] However, in the process of CO_2 electroreduction, there is a problem of the slow kinetic of CO_2 electroreduction, leading to wastage of energy and the insufficient utilization of sources.[2,3] Overcoming the challenges of CO_2 reduction under mild conditions would enable development of a broader portfolio of fuel-producing device. Therefore, the focal point is to develop efficient catalysts which can increase the activity and selectivity, especially for room-temperature CO_2 reduction in aqueous solutions.[4-6]

In the past few decades, researchers found that many metal oxide nanopowders could be the perfect catalysts in supercapacitors and/or lithium ion batteries for their controllable various morphologies.[7-10] This is because that different morphologies of the metal oxides might give different surface structures and surface areas, which then further influence the performance of electrochemical reaction. On the other hand, in the research field of electrochemical reduction of CO_2, Prakash reported[11] that taking Sn metal powder as the catalyst could give high current density and show high faradaic efficiency for produced formate in 0.5 M $NaHCO_3$ solution. Li[12] and Tang[13] *et al.*' find that the nanostructured surface of Cu metal plate could give more positive onset potential and higher current efficiency for CO_2 reduction in 0.5 M $NaHCO_3$ and 0.1 M $KClO_4$ aqueous solution, respectively. It is believed that the special morphology on the surface could provide abundant undercoordinated sites, which are more likely to be the active sites for CO_2 redcution.[6,12,13] As yet, the large overpotential was required for CO_2 reduction for many metal electrodes, resulting from the barrier associated with the initial electron transfer to form a $CO_2^{\bullet -}$ intermediate that is poorly stabilized by the metal electrode surfaces.[14] Most recently, it has been proposed that metastable metal oxides (e.g., SnOx) can participate in the

CO_2 reduction pathway on metal electrodes (e.g., Sn) by providing chemical functionality that stabilizes the incipient negative charge on CO_2 or by mediating the electron transfer directly, therefore the catalytic activity for CO_2 electroreduction was greatly enhanced relative to a bare metal electrode.[15] Although the potentials required for CO_2 reduction are past the standard reduction potentials for these oxides, metastable metal oxides are known to persist on electrode surfaces during cathodic reactions.[16] This suggests us a clue that metal oxides might be promising candidates for CO_2 reduction. Unfortunately, less is concern on the directly synthesized metal oxide nanocatalysts with different morphologies in CO_2 reduction, although the control of different special morphologies is very important on both activity and production selectivity in CO_2 reduction.

In this work, we report the synthesis of Cu_XO nanocatalysts with controlled different special morphologies by one-step hydrothermal method, which have the merits of low-cost, large-scale production and facile manipulation. By controlling the hydrothermal reaction conditions, various Cu_XO nanocatalysts with novel morphologies are received, such as hierarchical nanospheres with an average diameter of about 500 nm and solid microspheres in a large size of about 2.5 μm. In order to further investigate the effects of hydrothermal reaction time and temperature on the morphology and catalytic activity of as-prepared Cu_XO nanoparticles for CO_2 electroreduction, cyclic voltammetry (CV) study was utilized combining linear sweep voltammetry (LSV). For all electrochemical measurements, the Cu_XO nanoparticles were coated on the gas diffusion carbon paper to form target electrodes, in this way, easy diffusion path lengths can be achieved for substrates to access, leading to faster kinetics. At the same time, H_2 as byproduct which could impede the reduction reaction between CO_2 and electrode, could also be inhibited effectively.[11] The effect of catalyst loading was also tested by applying the gas diffusion layer (GDL) to make up a working electrode for CO_2 Electroreduction. The morphology effect on selectivity of formate production was studied systematically through faradaic efficiency combining production rate, which was examined by ion chromatography technique.

2. Experimental

2.1 Materials and catalyst synthesis

In this work, Copper(II) acetate monohydrate ($Cu(Ac)_2$) was used as precursor for Cu-oxide nanocatalyst preparation, which was provided by Sinopharm Chemical Reagent Co. (SCR) with 99% purity and, 2,5-dimethoxyaniline purchased from Ourchem Information Consulting Co. with 99% purity was used as the reducing agent in dilute aqueous solutions under hydrothermal conditions. In detail, 0.04 M $Cu(Ac)_2$ solution (40 mL) was mixed with 0.02 M 2,5-dimethoxyaniline solution (10 mL) till the mixture became dark green. During this process, a small amount of HAc (99%) was always added into $Cu(Ac)_2$ solution for avoiding the hydrolysis of $Cu(Ac)_2$. Then such mixture was transferred to a 100 mL Teflon-lined stainless steel autoclave. The autoclave was sealed and maintained at 180^{o}C for 1-15 hours or at 160 -220^{o}C for 2 hours, respectively, in order to clarify the optimal reaction condition. The final powder was washed by ethanol and dried overnight. In this way, Cu_XO nanocatalysts with different morphologies were synthesized as shown in Fig. 1. For a convenient discussion, the resulting catalysts were labeled as $Cu_XO_{T\text{-}\tau}$, where T indicates the temperature (^{o}C) used for hydrothermal reaction and τ the time (h) of hydrothermal reaction. As an example, the Cu_XO catalyst synthesized at 180^{o}C for 2 hours was expressed as $Cu_XO_{180\text{-}2}$ and so on.

2.2 Electrode preparation and electrochemical test

For all electrochemical measurements, the Cu_XO nanoparticles were coated on the gas diffusion carbon paper to form target electrodes. For catalyst ink preparation, Cu_XO nanocatalyst (15 mg) was suspended in 200 μL isopropyl alcohol (Sinopharm Chemical Reagent Co.) and 5 wt% Nafion® solution (100 mg) was dropped in order to improve adhesion of catalyst ink. For exploring the effect of catalyst loading on catalytic activity, 10 mg, 15 mg and 20 mg catalysts were dispersed in 200 μL isopropyl alcohol to form different loadings of catalyst inks (2 mg cm^{-2}, 3 mg cm^{-2} and 4 mg cm^{-2}, about 80% of the catalyst powders were coated on the electrode),

respectively. A gas diffusion layer (GDL) (4 cm^2 Toray carbon paper, TGP-H-090) with catalysts coated on was used as the working electrode and tested in a conventional three-electrode electrochemical H-type cell, in which a piece of Nafion® 117 cation exchange membrane (H^+ form) as a separator, a platinum foil electrode as the counter electrode and a saturated calomel electrode (SCE) as the reference electrode. All measured potentials were referenced to a standard hydrogen electrode (SHE). A CH Instruments 600E was used for all electrochemical experiments. An aqueous electrolyte (0.5 M $KHCO_3$) was used as the measurement solution, which was bubbled with 1.0 atm CO_2 gas (99.99%) for 30 minutes for the CO_2 reduction measurements. The electrocatalytic activity and kinetics of the working electrode was tested using cyclic voltammetry (CV) and linear sweep voltammetry (LSV) at a scan rate of 100 mV s^{-1} and 5 mV s^{-1}, respectively, in the potentials ranging from 1.25 V to -1.25 V. All these tests were carried out at ambient temperature and pressure.

2.3 Physical characterization and reduction product measurement

The scanning electron microscopy (SEM) images of samples were taken by Zeiss ultra plus thermal field emission SEM instrument (Carl Zeiss SMTAG, Germany). High-resolution transmission electron microscopy (HR-TEM) analyses were performed with a high-resolution Hitachi JEM-2100F operating at 200 kV to obtain information of the average particle size and the morphology difference of catalysts. The crystal-phase X-ray diffraction (XRD) patterns of typical Cu_XO catalysts were obtained using a Philips PW3830 X-ray diffractometer equipped with Cu-Ka radiation (λ=0.15406 nm). The intensity data were collected at 25°C in the 2θ range from 0° to 90° with a scan rate of 1.20°min^{-1}. Brunauer-Emmett-Teller (BET) specific surface area was characterized by nitrogen adsorption in a Micromeritics ASAP 2020 nitrogen adsorption apparatus (USA). The product solution was filtered with filter membrane (0.22 μm) and the $HCOO^-$ concentration was determined by ion chromatography (ICS-90, Dionex, USA) using an AS14 4 mm × 250 mm separation column at a flow rate of 1 ml/min. The mobile phase was a mixed aqueous solution of Na_2CO_3 (4.5 mM) and $NaHCO_3$ (0.8 mM), and a H_2SO_4 (20 mM) aqueous solution was used as a

regenerator.

3. Results and discussion

3.1 Effect of hydrothermal reaction condition on the morphology of Cu_XO nanocatalysts

To observe the morphology changes under different hydrothermal conditions, Fig. 1 shows SEM images of the Cu_XO nanocatalysts synthesized at 180°C for 2, 5, 10 and 15 hours, respectively. It can be seen that $Cu_XO_{180\text{-}2}$ catalyst indicates a clear 3-dimensioned (3D) hierarchical nanosphere structure with an average diameter of about 500 nm (Fig. 1(a)). After a careful observation, it was found that such nanospheres are comprised of secondary structures which are made up of laminated small nanosheets with an average diameter of about 50 nm. With increasing the synthesis time to 5 hours, however, a little deformation of the secondary structure was observed for $Cu_XO_{180\text{-}5}$ catalyst, where the slender nanorods with the diameter of about 20 nm and 50 nm are formed. Although the morphology with hierarchical nanosphere structure is still maintained, the diameter of the nanosphere increased to about 800 nm (Fig. 1(b)). Further increasing the hydrothermal reaction time to 10 hours induces the formation of inner hollow nanosphere structure for $Cu_XO_{180\text{-}10}$, ie., the 3D hierarchical nanosphere structure tends to break at this stage (Fig. 1(c)). Finally, when the reaction time was further increased to 15 hours, the 3D structure of $Cu_XO_{180\text{-}15}$ catalyst completely collapsed. During this process, large amounts of nanoparticles with a diameter of 50 nm clustered together and, most of the nanoparticles were wrapped by amorphous substance which was inherited from the precursors as shown in Fig. 1(d). Normally, the fabrication process of these nanostructures in Fig. 1(a-c) can be explained by a self-transformation process of the metastable aggregated particles accompanied by the Ostwald ripening[17-19], where the time of hydrothermal reaction plays a key role in obtaining the special morphology of the catalyst.

It is interesting to find that when the temperature for hydrothermal reaction was

increased from 180°C to 220°C while still maintaining the reaction time for 2 hours, dense microspheres are formed for $Cu_XO_{220\text{-}2}$ catalyst with a large size in diameter of 2.5 μm (Fig. 1(e)), which is very different from the morphology of $Cu_XO_{180\text{-}2}$ catalyst (Fig. 1(a)). Further from the high-resolution SEM image of $Cu_XO_{220\text{-}2}$ (Fig. 1(f)), it was found that the surface of these large mircrospheres are comprised of small nanorods with an average diameter of 25 nm, which are densely arrayed with sporadic cavities in the intervals of these nanorods. These morphology changes may greatly influence the catalytic activity of the catalysts for CO_2 electroredcution, which will be discussed thoroughly in the following section.

For further clarifying the morphology differences of Cu_XO catalysts, HR-TEM (Fig. 2) combining XRD patterns (Fig. 3) were used to investigate $Cu_XO_{180\text{-}2}$, $Cu_XO_{180\text{-}15}$, $Cu_XO_{220\text{-}2}$, which are representatives in all Cu_XO catalysts. From Fig. 2(a), it can be seen clearly that $Cu_XO_{180\text{-}2}$ catalysts are flabby nanospheres which are made up of small nanosheets. The corresponding fast Fourier transformation (FFT) pattern (inset of Fig. 2(a)) exhibited rings with several obviously brighter dots, indicating their polycrystalline characteristics. The HR-TEM image shown in Fig. 2(b) combing XRD patterns in Fig. 3(a) provides more detailed structural information of the $Cu_XO_{180\text{-}2}$ catalyst. The lattice fringes showed a lattice spacing of 0.27 nm (Fig. 2(b)), corresponding to the {-111} planes of CuO. Fig. 2(c) shows the TEM image of $Cu_XO_{180\text{-}15}$, which correlates well with the SEM image (Fig. 1(d)), where the $Cu_XO_{180\text{-}15}$ catalysts did not show any special morphology, ie., with the increase of synthesis time high up to 15 hours, the nanosphere structure was destructed completely, and the morphology of $Cu_XO_{180\text{-}15}$ turned to scattered 1-dimension nanoparticles which were covered by amorphous substance. Therefore the FFT pattern shown in the inset of Fig. 2(c) does not show obvious brighter dots. However, in Fig. 2(d), by HR-TEM and calculation of XRD pattern, the lattice fringes on scattered nanoparticles were related to {110} planes of Cu_2O. The morphology of $Cu_XO_{220\text{-}2}$ shown in Fig. 2(e) also has a well consistent result with the SEM image as shown in Fig. 1(e) and (f). The FFT pattern (inset of Fig. 2(e)) combing HR-TEM (Fig. 2(f)) indicates that the $Cu_2O_{220\text{-}2}$ was also polycrystalline copper and the lattice spacing is

0.21 nm (Fig. 2(f)), indicating a relationship with {200} planes of Cu_2O. All the clear crystalline information of $Cu_XO_{180\text{-}2}$, $Cu_XO_{180\text{-}15}$ and $Cu_XO_{220\text{-}2}$ was shown in Fig. 3.

In Table 1, all the BET specific surface areas are summarized related to the different catalysts' morphology, their average particle size and electrochemically active surface area. One can see that $Cu_XO_{180\text{-}2}$ catalyst has the largest specific surface area of 63.50 $m^2\ g^{-1}$, $Cu_XO_{180\text{-}15}$ has the specific surface area of 53.62 $m^2\ g^{-1}$, while $Cu_XO_{220\text{-}2}$ has the smallest specific surface area of 22.16 $m^2\ g^{-1}$, which are ascribed to their structural difference. Based on the observations, it is reasonable to conclude that the largest surface area of $Cu_XO_{180\text{-}2}$ results from the loose and hierarchical nanosphere structure. For $Cu_XO_{180\text{-}15}$, the nanosphere structure was destroyed, and the catalyst was made up of clustered nanosheets, thus the BET surface area of $Cu_XO_{180\text{-}15}$ decreased correspondingly. However, for $Cu_XO_{220\text{-}2}$, the small surface area comes from the large size of microsphere structure which was densely arrayed by small nanorods.

The electrochemically active surface area was examined by the double layer capacitance in N_2-saturated 0.1 M $HClO_4$. The CV was measured in a potential range without Faradaic process occurred and, the capacitance, C (F), was calculated by the equation C = current density/scan rate. As shown in Table 1, the $Cu_XO_{180\text{-}2}$ with the special laminated nanosphere structure showed the best capacitance, and the capacitance of $Cu_XO_{220\text{-}2}$ (microsphere structure) was just a little minor than that of $Cu_XO_{180\text{-}2}$. Although the BET surface area of $Cu_XO_{220\text{-}2}$ is the smallest in the tested three catalyst samples, the 3D sphere morphology of $Cu_XO_{220\text{-}2}$ and the results of the electrochemically active surface area indicate that the sphere nanostructure might be competitive to give more active sites in CO_2 electroreduction, as will be demonstrated below. These results could explain that why the catalytic activity of $Cu_XO_{180\text{-}2}$ and $Cu_XO_{220\text{-}2}$ is high for CO_2 electroreduction from one hand. However, for the $Cu_XO_{180\text{-}15}$ catalyst without any special morphology, the capacitance is only 300, which is about one-third smaller than that of $Cu_XO_{180\text{-}2}$. These results are in line with the conclusions in Fig.1-3.

3.2 Electrochemical activities of catalyzed CO_2 reduction

For clarifying the effects of hydrothermal conditions including reaction time and temperature on the catalysts' activities of catalyzed CO_2 eletroreduction, Fig. 4 shows CV responses of CO_2 saturated 0.5 M $KHCO_3$ solution on four catalysts coated on GDL, ie., $Cu_XO_{180\text{-}1}$, $Cu_XO_{180\text{-}2}$, $Cu_XO_{180\text{-}5}$, $Cu_XO_{180\text{-}10}$ and $Cu_XO_{180\text{-}15}$, respectively. From Fig. 4 (a), it can be seen that the $Cu_XO_{\text{-}180\text{-}2}$ catalyst resulted in the earliest onset potential (about -0.55 V vs. SHE) in all tested catalyst samples and then the $Cu_XO_{180\text{-}5}$ catalyst if the catalytic current obtained from Cu_XO to its reduction state (at the end of reduction peak at the negative potential direction in Fig. 4 was ignored. However, for either $Cu_XO_{180\text{-}1}$ or $Cu_XO_{180\text{-}10}$ and $Cu_XO_{180\text{-}15}$ catalysts, their onset potentials appear at about -0.85 V vs. SHE, which are more 300 mV negative shift compared to that of $Cu_XO_{180\text{-}2}$. Moreover, at the most negative potentials, the cathodic current density is much larger for $Cu_XO_{180\text{-}2}$ catalyst than the catalysts synthesized at 180^{o}C for longer times. This suggests that hydrothermal reaction at 180^{o}C for 2 hours is the optimal condition for Cu_XO catalyst, under which the morphology of 3D hierarchical nanospheres with secondary structures for $Cu_XO_{180\text{-}2}$ can be well formed. Such special morphology may provide larger active surface area and more active sites for CO_2 electroreduction, thus the improved catalytic activity of $Cu_XO_{180\text{-}2}$ catalyst toward CO_2 reduction. As described in Fig. 2(a-d), when the hydrothermal reaction time was increased while maintain the synthesis temperature unchanged (at 180^{o}C), such hierarchical structure was destroyed and no more 3D structure left at last, instead, the $Cu_XO_{180\text{-}15}$ is only consisted of clustered nanosheets. Obviously, the decreased catalytic activity of $Cu_XO_{180\text{-}10}$ and $Cu_XO_{180\text{-}15}$ might be partly resulted from the destroyed hierarchical nanoshpere structure.[20] It should be mentioned that the $Cu_XO_{220\text{-}2}$ catalyst also shows a comparably better performance for CO_2 reduction (Fig. 4(b)). The onset potential of $Cu_XO_{220\text{-}2}$ catalyst is very similar to that of $Cu_XO_{180\text{-}2}$ catalyst under the same the measuring conditions. Additionally, the current density at the most negative potential for $Cu_XO_{220\text{-}2}$ catalyst is even larger than that for $Cu_XO_{160\text{-}2}$ and $Cu_XO_{200\text{-}2}$ catalysts, while is only slightly less than that of $Cu_XO_{180\text{-}2}$. These results imply that the microsphere morphology of $Cu_XO_{200\text{-}2}$ could not be

perfect as the special hierarchical nanosphere of $Cu_XO_{180\text{-}2}$ because of the large size and dense structure of the former when compared to the fluffy structure of the latter, of which the dense microsphere morphology of $Cu_XO_{200\text{-}2}$ may not easily offer more active sites for catalytic CO_2 reduction than $Cu_XO_{180\text{-}2}$, however, because of the 3D nanosphere structure of $Cu_XO_{200\text{-}2}$, the activity of $Cu_XO_{200\text{-}2}$ is still higher than that of $Cu_XO_{180\text{-}15}$ (without special morphology). Note that the overpotential of CO_2 electroreduction of the optimal $Cu_XO_{180\text{-}2}$ was found to be at -0.55 V vs. SHE, which is much lower than those for metal Cu electrodes (about 450 mV positive shift) reported elsewhere.[21-23] Even for those Cu_XO nanocatalysts (e.g., $Cu_XO_{180\text{-}10}$ and $Cu_XO_{180\text{-}15}$) with comparably lower activities in this work, their overpotentials of -0.85 V vs. SHE is still nearly 150 mV more positive shift than the reported ones.[21-23]

3.3 Faradaic efficiency of the produced formate

To further confirm that the morphology structures could have effect on the catalytic activity and production selectivity towards CO_2 reduction, the produced formate was determined and analyzed as a target by ion chromatography (IC), after applying a constant potential of -0.7 V vs. SHE in CO_2 saturated 0.5 M $KHCO_3$ electrolyte for 60 minutes. The faradaic efficiency was calculated using the following equation:[24]

$$\eta_{formate} = \frac{n_{formate} 2F}{C} \qquad (1)$$

Where $n_{formate}$ is the mole number of produced formate, F is the faradaic constant, and C is total coulomb of electrons passed across the electrode during the electrolysis. Fig. 5(a) and (b) show the total reduction current density as a function of operation time for all tested catalyst samples, which was measured at -0.7 V vs. SHE. As expected, the $Cu_XO_{180\text{-}2}$ catalyst gives the highest reduction current density when compared with other Cu_XO catalysts synthesized at different hydrothermal conditions. Further from Fig. 6, it can be clearly seen that the highest faradaic efficiency obtained in this work reached high up to ~59% for the $Cu_XO_{180\text{-}2}$ hierarchical nanospheres,

which is remarkably improved at low overpotential (-0.55 V vs. SHE) compared to those reported elsewhere.[12,21,25,26] However, the faradaic efficiency sharply decreased along with the longer hydrothermal reaction time regardless of the synthesis temperature applied. This demonstrates further that the catalytic activity for CO_2 electroreduction strongly depends on the surface morphology of the catalysts as-prepared. For a good comparison, all the detailed results of faradaic efficiency are presented in Table 2. It can be seen that only the two catalysts of $Cu_XO_{180\text{-}2}$ and $Cu_XO_{180\text{-}5}$ have the faradaic efficiencies exceeding 30%, which is in a well agreement with CV results as shown in Fig. 4. As discussed above, these two catalysts, particular to $Cu_XO_{180\text{-}2}$, process the novel morphologies which may offer large surface area and more active sites in catalyzed CO_2 reduction (Table 1), thus the large enhancement in catalytic performance for CO_2 electroreduction. Further from Table 2, it was noted the $Cu_XO_{180\text{-}2}$ has the best selectivity for formate among all the Cu_XO catalysts synthesized. This result, along with the CV results as shown in Fig. 4 further suggests that catalyst's morphology is a major factor that cannot be ignored in CO_2 reduction, and the special hierarchical nanosphere structure is more effective for electrochemical reduction of CO_2 in this work.

Production rate combining the faradaic efficiency and current density could also be used to contrast the performance of different Cu_XO catalysts. Fig. 7 combing Table 2 shows the detailed production rate for each Cu_XO catalyst. Evidently, the $Cu_XO_{180\text{-}2}$ has the best performance compared to Cu_XO catalysts made by other conditions. From Fig. 7, the production rate of $Cu_XO_{180\text{-}2}$ is about one order higher than the other Cu_XO catalysts and follows the order: $Cu_XO_{180\text{-}2} >> Cu_XO_{180\text{-}5} > Cu_XO_{180\text{-}10} > Cu_XO_{180\text{-}15}$, and $Cu_XO_{180\text{-}2} >> Cu_XO_{220\text{-}2} > Cu_XO_{200\text{-}2} > Cu_XO_{160\text{-}2}$, which are synthesized for Cu_XO both at a longer reaction time or at a higher temperature of 220°C and lower temperature of 160°C (Table 2). All of these results of formate production rate are consist well with the results of faradaic efficiency. Based on the above observations we could give a schematic of the structures of the typical $Cu_XO_{180\text{-}2}$, $Cu_XO_{180\text{-}15}$ $Cu_XO_{220\text{-}2}$ and the morphology effect on the active surface area and formate faradaic efficiency. This could help us to have a more clearly mechanistic understanding on

why and how the structures are affecting the electrocatalytic activities. As seen in Fig. 8, both the Cu_XO_{180-2} and Cu_XO_{220-2} were consisted of secondary structures which provide them larger active surface area and higher faradaic efficiency than Cu_XO_{180-15} with only 1-dimensional structure. However, the diameter of Cu_XO_{220-2} was fairly large and catalyst sphere was 4 times bigger than that of Cu_XO_{180-2}. That is why the faradaic efficiency of Cu_XO_{220-2} was not that perfect as Cu_XO_{180-2}. Therefore, the morphology is a key factor in determining the activity and selectivity of catalysts and, the synthesis reaction time and temperature could effectively turning the catalysts' morphology and thus their catalytic performance.

3.4 Loading effect on the activity and selectivity for CO_2 catalytic reduction

For low-cost Cu-based catalyst, increasing the catalyst loading obviously could be a way to improve its catalytic performance. Loading effect has been widely discussed in the field of fuel cell, [27-29] however, for CO_2 electroreduction, the effect of catalyst loading has never been reported yet. Based on this consideration, the loading effect on catalytic activity of CO_2 electroreduction is investigated by CV curves, with the most efficient Cu_XO_{180-2} catalyst as a typical candidate. As shown in Fig. 9 (a), both the onset potential and the current density at the most negative potential are greatly enhanced with increasing catalyst loading from 2 mg cm^{-2} to 3 mg cm^{-2} (with 300 mV positively shifted onset potential and 2.5 times increased current density). When the loading is further increased to 4 mg cm^{-2}, both onset potential and current density are retreated to the level of 2 mg cm^{-2} loading. From what has been discussed above, it could be concluded that 3 mg cm^{-2} is the optimal catalyst loading for CO_2 electroreduction.

To further verify the loading effect on the performance of catalytic CO_2 reduction, Fig. 9(b-d) combing Table 2 exhibit the current density, faradaic efficiency and production rate for different catalyst loadings. It can be obviously seen that the current density for catalyst loading of 3 mg cm^{-2} is much higher than for other two, and 2.2-fold of 4 mg cm^{-2} loading and 3.7-fold of 2 mg cm^{-2} loading, respectively (Fig. 9(b)). Furthermore, both the faradaic efficiency (Fig. 9(c)) and production rate (Fig.

9(d)) of formate reach the maximum under the loading of 3 mg cm^{-2} which are in accord with what concluded in Fig. 9 (a) that the loading of 3 mg cm^{-2} is the optimal one.

Regarding the catalyst loading, there has not a clarified mechanism on its prompting and/or probhibiting effect. However, it is reasonable to be viewed that this loading effect could provide more active sites available for reducing initial electron transfer to form a CO_2•− intermediate that is poorly stabilized by the metal electrode surfaces, that is, increasing the catalyst loading may lead to an enhanced electron pathway in CO_2 reduction process. Another explanation may be considered, that is, at low loading, the catalyst layer is so thin that the generated CO_2•− intermediate have no enough time to stay to find neighboring active site for next reduction process, while at high catalyst loading, CO_2•− intermediate could have longer time to remain in catalyst layer, thus more chance for the reduction of CO_2•− intermediate further to formate. However, too high loading will cause the catalyst layer too thick, leading to the easy cracking and falling off of the catalyst from the electrode as well as larger electric resistance, thus resulting in lower catalytic activity. And this has been well demonstrated for cathodic catalyst for oxygen reduction reaction in fuel cells.[27-29]

4. Conclusions

The effects of hydrothermal conditions on the morphology formation of Cu_XO nanocatalysts and their influences for catalytic performance in CO_2 electroreduction were investigated. It was found that hydrothermal reaction at 180^oC for 1-15 or at 160 -220^oC for 2 hours could induce the formation of sphere-like nanostructure. However, the special 3D hierarchical nanospheres (~500 nm) comprised of secondary structures could only be received at 180^oC for 2 hours. This condition performs best for Cu_XO catalysts in CO_2 catalytic reduction in terms of both catalytic activity and selectivity, under which the faradaic efficiency of formate could realize ~59%, and the production rate is one order increased than Cu_XO synthesized under other conditions. However, the special hierarchical nanospheres were destroyed with increasing the hydrothermal

reaction time, and at the same time, the reduction activity and production faradaic efficiency decreased greatly, suggesting that surface morphology control of the catalyst is a significant factor, which determines the active sites and surface area and even pathway for CO_2 reduction reaction. The catalyst loading effects on CO_2 electroreduction have also been investigated in this paper. It was concluded that under the loading of 3 mg cm^{-2}, the $Cu_XO_{180\text{-}2}$ performs the high catalytic activity and, the overpotential of CO_2 reduction is -0.55 V vs. SHE, which is nearly 450 mV positive shift than previous works.

Acknowledgement

This work was supported by the National Natural Science Foundation of China (21173039); Specialized Research Fund for the Doctoral Program of Higher Education, SRFD (20110075110001) of China; the Innovation Program of the Shanghai Municipal Education Commission (14ZZ074), International Academic Cooperation and Exchange Program of Shanghai Science and Technology Committee (14520721900), the Graduate degree thesis Innovation Foundation of Donghua University (EG2014014) and College of Environmental Science and Engineering, State Environmental Protection Engineering Center for Pollution Treatment and Control in Textile Industry, Donghua University,. All the financial supports are gratefully acknowledged.

References

1 J. L. Qiao, Y. Y. Liu, F. Hong, J. J. Zhang, *Chem. Soc. Rev.*, 2014, **43**, 631-675.

2 M. Gattrell, N. Gupta, A. Co, *J. Electroanal. Chem.*, 2006, **594**, 1-19.

3 N. S. Spinner, J. A. Vega, W. E. Mustain, *Catal. Sci. Technol.*, 2012, **2**, 19-28.

4 P. Kang, T. J. Meyer, M. Brookhart, *Chem. Sci.*, 2013, **4**, 3497–3502.

5 Y. Chen, C. W. Li, M. W. Kanan, *J. Am. Chem. Soc*., 2012, **134**, 19969−19972.

6 J. L. Qiao, P. Jiang, J. S. Liu, J. J. Zhang, *Electrochem. Commun.*, 2014, **38**, 8–11.

7 Y. Tan, X. Xue, Q.Peng, H. Zhao, T. Wang, Y. Li, *Nano Lett.*, 2007, **7**, 3723-3728.

8 Z. Liu, Y. Yang, J. Liang, Z. Hu, S. Li, S. Peng, Y. Qian, *J. Phys. Chem. B*, 2003, **107**, 12658-12661

9 Y. Jiao, F. Wang, X. Ma, Q. Tang, K. Wang, Y. Guo, L. Yang, *Microporous Mesoporous Mater.*, 2013, **176**, 1-7.

10 C. D. Lokhande, D. P. Dubal, O. S. Joo, *Curr. Appl. Phys*., 2011, **11**, 255-270.

11 G. K. S. Prakash, F. A. Viva, G. A. Olah, *J. Power Sources*, 2013, **223**, 68-73.

12 C. W. Li and M. W. Kanan, *J. Am. Chem. Soc*., 2012, **134**, 7231-7234

13 W. Tang, A. A. Peterson, A. S. Varela, Z. P. Jovanov, L. Bech, W. J. Durand, S. Dahl, J. K. Norskov, I. Chorkendorff, *Phys. Chem. Chem. Phys.*, 2012, **14**, 76-81.

14. M. Gattrell, N.Gupta, A. Co, *J. Electroanal. Chem*., 2006, **594**, 1.

15. Y. Chen, M. W. Kanan, *J. Am. Chem.Soc*., 2012, **134**, 1986−1989

16 D. Rochefort, P. Dabo, D. Guay, P. M. A. Sherwood, *Electrochim. Acta*, 2003, **48**, 4245.

17 J. J. Teo, Y. Chang, H. C. Zeng, *Langmuir*, 2006, **22**, 7369-7377.

18 F. Behnoudnia, H. Dehghani, *Polyhedron*, 2013, **56**, 102-108.

19 J. Li, H. C. Zeng, *J. Am. Chem. Soc.*, 2007, **129**, 15839-15847.

20 H. Zhang, J. Feng, M. Zhang, *Mater. Res. Bull.*, 2008, **43**, 3221-3226.

21 J. Lee, Y. Tak, *Electrochim. Acta*, 2001, **46**, 3015-3022.

22 P. Jiang, J. L. Qiao, M. Y. Fan, C. Y. Ma, J. S. Liu, *ECS Trans.*, 2013, **53**, 71-77.

23 P. Jiang, J. L. Qiao, M. Y. Fan, C. Y. Ma, J. S. Liu, *ECS Trans.*, 2013, **58**, 91-97.

24 J. Wu, F. G. Risalvato, F. S. Ke, P. J. Pellechia, X. D. Zhou, *J. Electrochem. Soc.*, 2012, **159**, F353-F359.

25 Y. Hori, A. Murata, R. Takahashi, *J. Chem. Soc., Faraday Trans. 1*, 1989, **85**, 2309-2326.

26 Y. Hori, K. Kikuchi, S. Suzuki. *Chem.Lett*., 1985, **53**, 1695.

27 G. Lalande, R. Côté, G. Tamizhmani, D. Guay, J. P. Dodelet, *Electrochim. Acta*, 1995, **40**, 2635-2646.

28 G. Lalande, G. Tamizhmani, R. Côté, L. Dignard-Bailey, M. L. Trudeau, R. Schulz, D. Guay, J. P. Dodelet, *J. Electrochem. Soc.*, 1995, **142**, 1162-1168.

29 L. Ding, J. L. Qiao, X. F. Dai, J. Zhang, J. J. Zhang, B. L. Tian, *Int. J. Hydrogen Energy*, 2012, **37**, 14103-14113.

Figure captions

Fig. 1 SEM images of (a) $Cu_XO_{180\text{-}2}$, (b) $Cu_XO_{180\text{-}5}$, (c) $Cu_XO_{180\text{-}10}$, (d) $Cu_XO_{180\text{-}15}$, (e) $Cu_XO_{220\text{-}2}$. (f) High-resolution SEM image of $Cu_XO_{220\text{-}2}$.

Fig. 2 TEM images and corresponding FFT pattern (inset) of typical (a) $Cu_XO_{180\text{-}2}$, (c) $Cu_XO_{180\text{-}15}$, (e) $Cu_XO_{220\text{-}2}$. High-resolution TEM images of (b) $Cu_XO_{180\text{-}2}$, (d) $Cu_XO_{180\text{-}15}$, (f) $Cu_XO_{220\text{-}2}$.

Fig. 3 XRD patterns of typical (a) $Cu_XO_{180\text{-}2}$, (b) $Cu_XO_{180\text{-}15}$, (c) $Cu_XO_{220\text{-}2}$.

Fig. 4 Current-potential curves of CO_2 reduction measured in CO_2-saturated 0.5 M $KHCO_3$ solution on Cu_XO nanocatalysts synthesized at (a) 180°C for 1-15 hours and (b) 160-220°C for 2 hours. Potential scan rate: 100 mV s^{-1}. Catalyst loading: 3 mg cm^{-2}.

Fig. 5 Current-time curves for Cu_XO nanocatalysts synthesized at (a) 180°C for 2-15 hours and (b) 160-220°C for 2 hours. Catalyst loading: 3 mg cm^{-2}.

Fig. 6 Faradaic efficiency of produced on Cu_XO nanocatalysts synthesized at (a) 180°C for 2-15 hours and (b) 160-220°C for 2 hours. Catalyst loading: 3 mg cm^{-2}.

Fig. 7 Production rate of Cu_XO nanocatalysts synthesized at (a) 180°C for 2-15 hours and (b) 160-220°C for 2 hours. Catalyst loading: 3 mg cm^{-2}.

Fig. 8 Schematic structures of typical $Cu_XO_{180\text{-}2}$, $Cu_XO_{180\text{-}15}$, $Cu_XO_{220\text{-}2}$ and, the structure effect on the active surface area and formate faradaic efficiencies.

Fig. 9 (a) Current-potential curves of CO_2 electroreduction for different catalyst loadings. Potential scan rate: 100 mV s^{-1}. (b) Current-time curves for various catalyst loadings. (c) Faradaic efficiency and (d) Production rate of different catalyst loadings.

The Cu_XO catalyst is synthesized at 180°C for 2 hours ($Cu_XO_{180\text{-}2}$), and catalyst loading: 2~4 mg cm^{-2}.

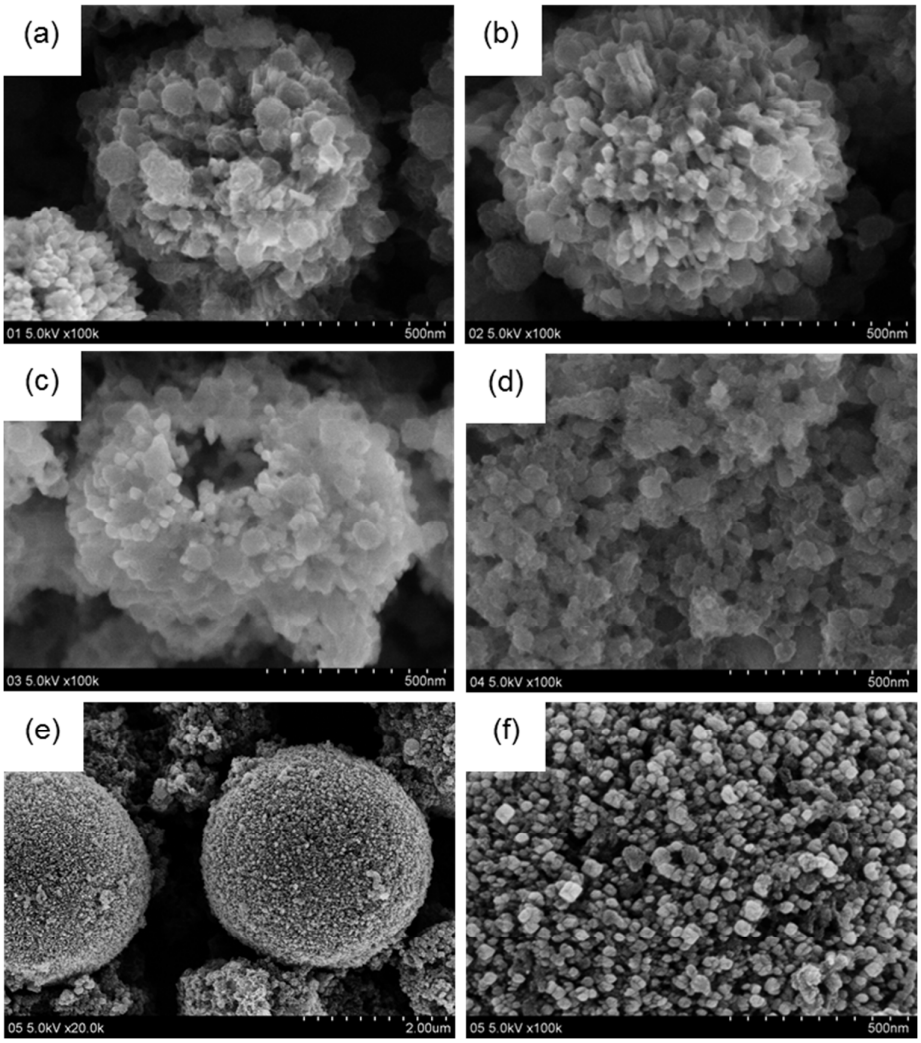

Fig. 1

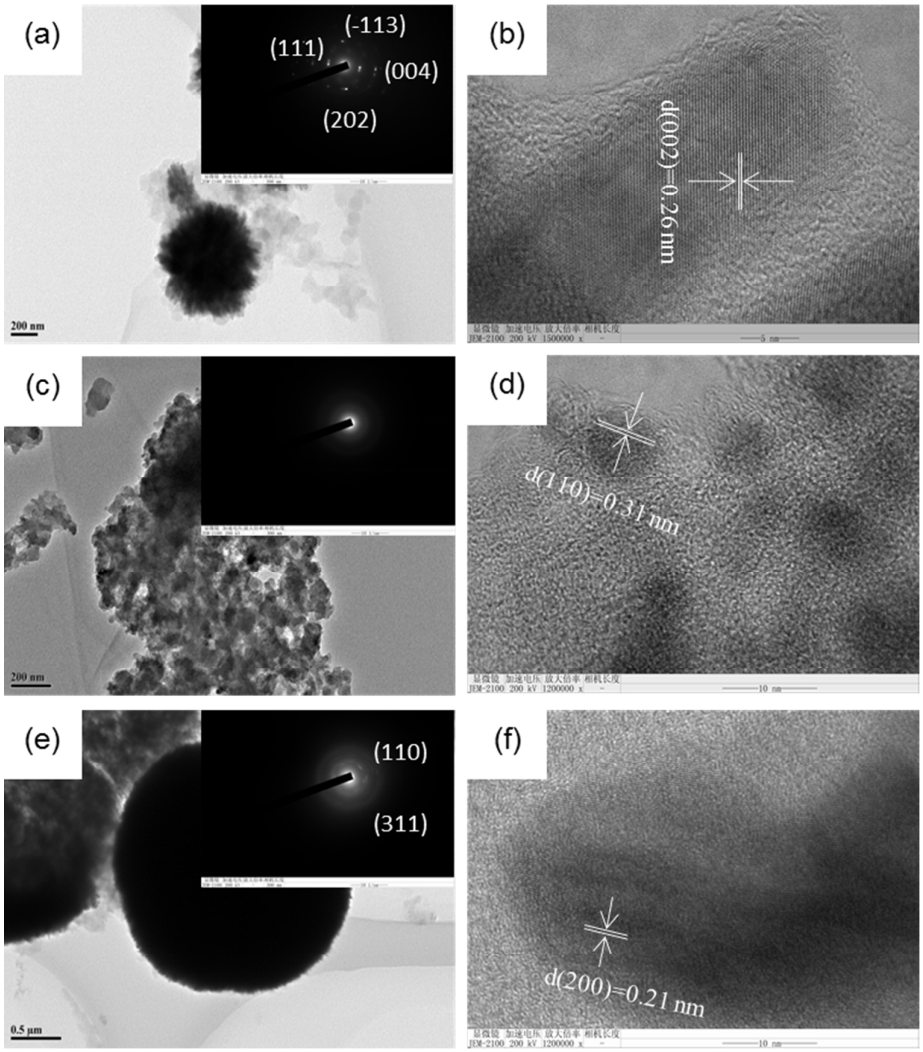

Fig. 2

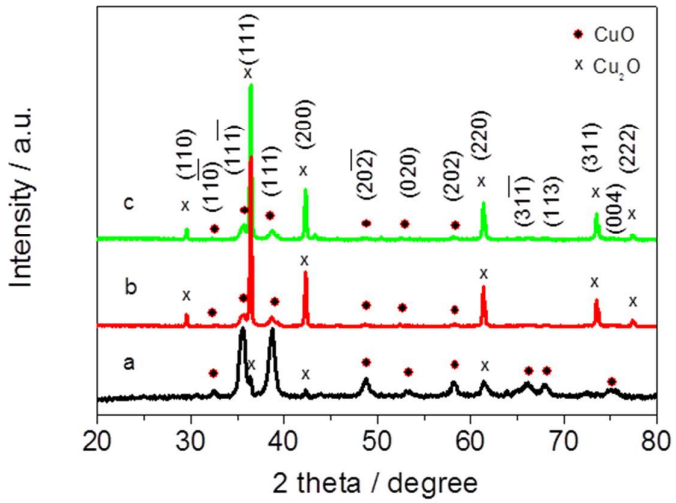

Fig. 3

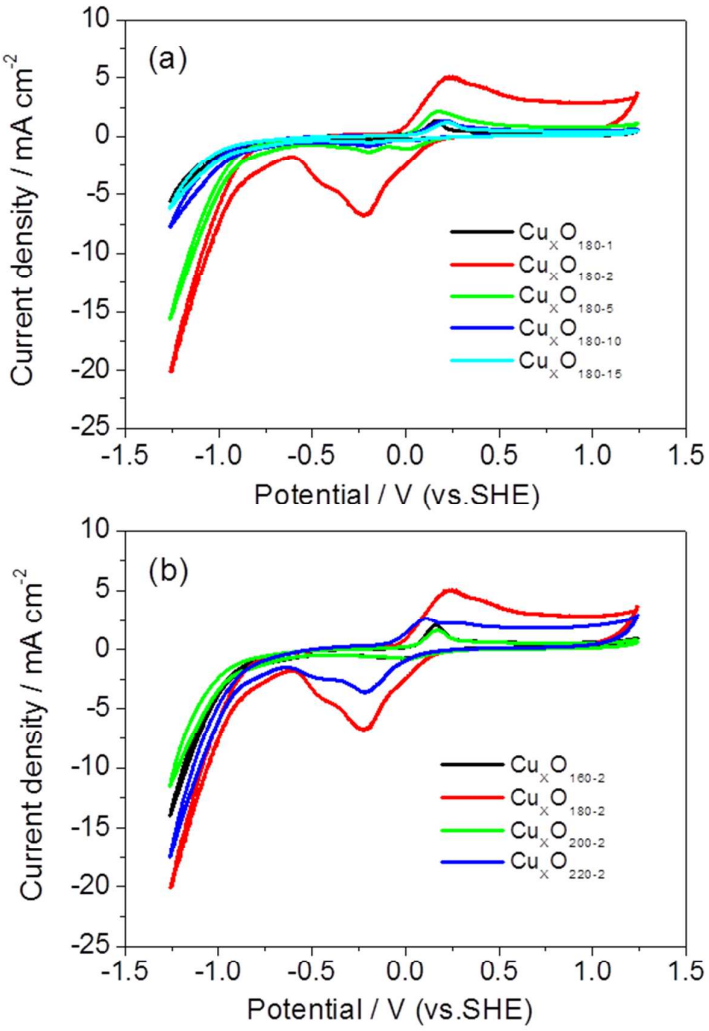

Fig. 4

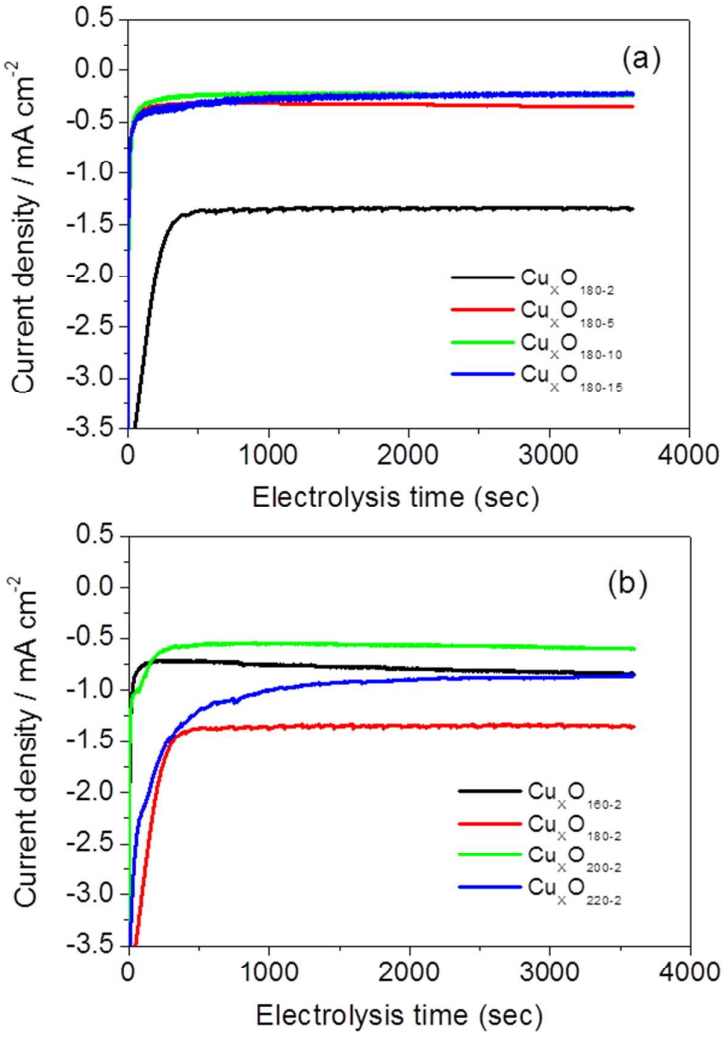

Fig. 5

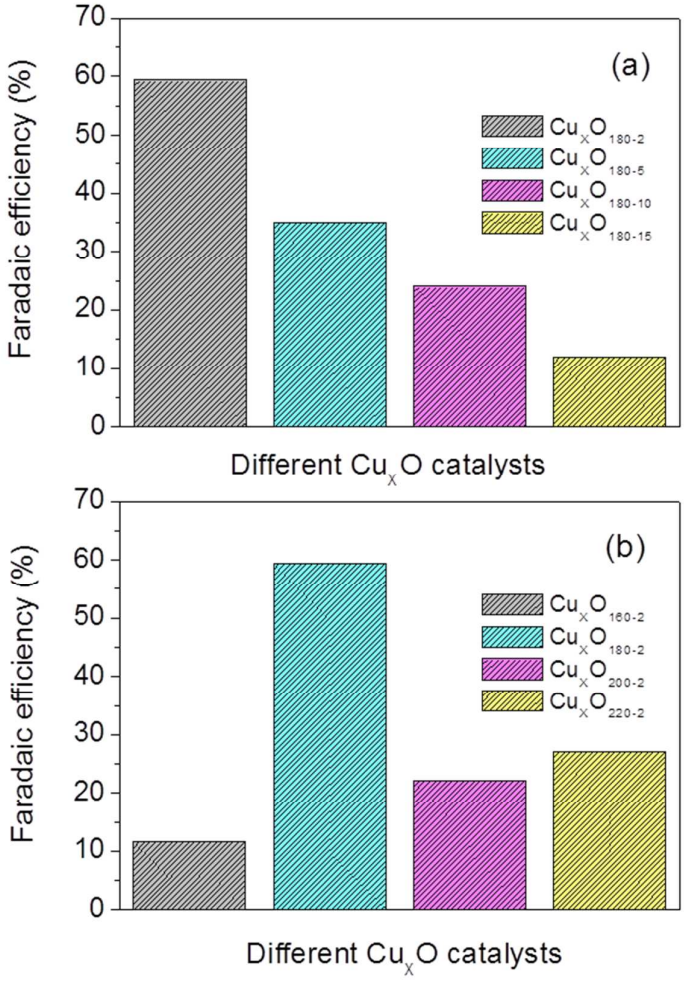

Fig. 6

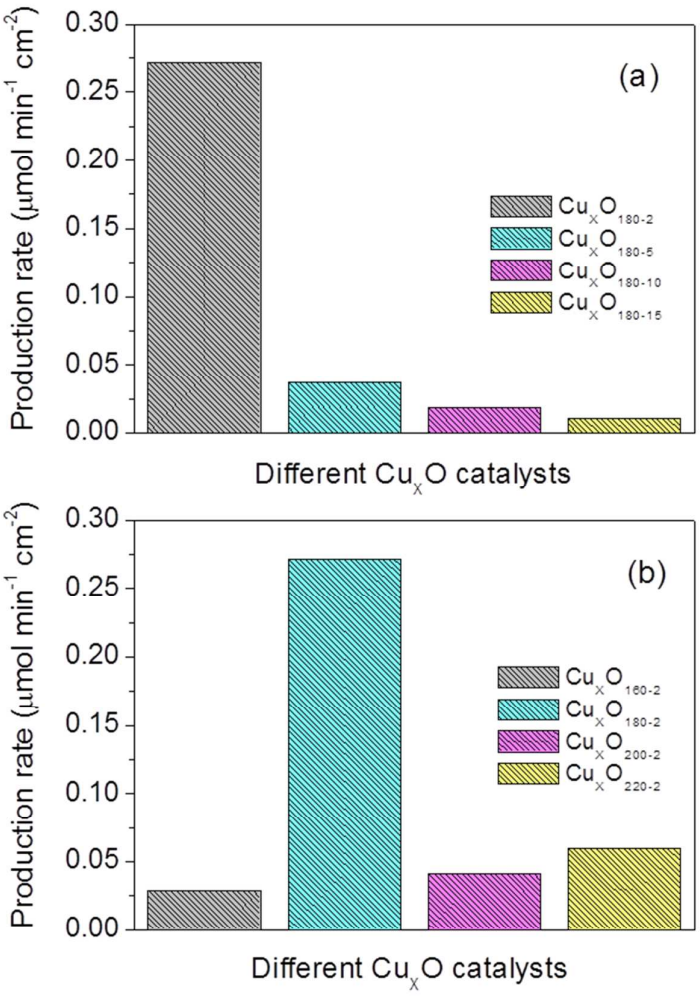

Fig. 7

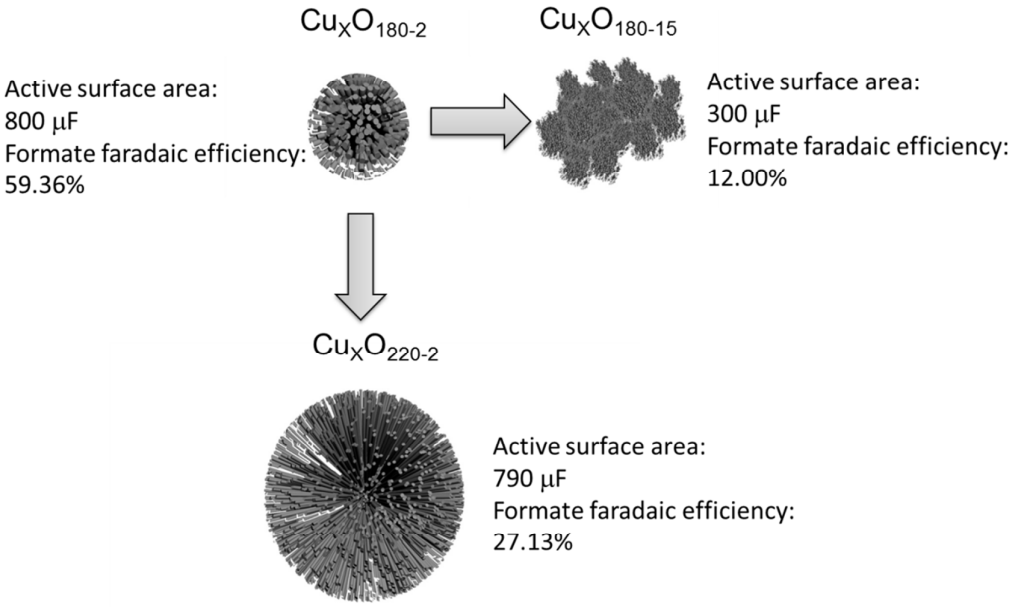

Fig. 8

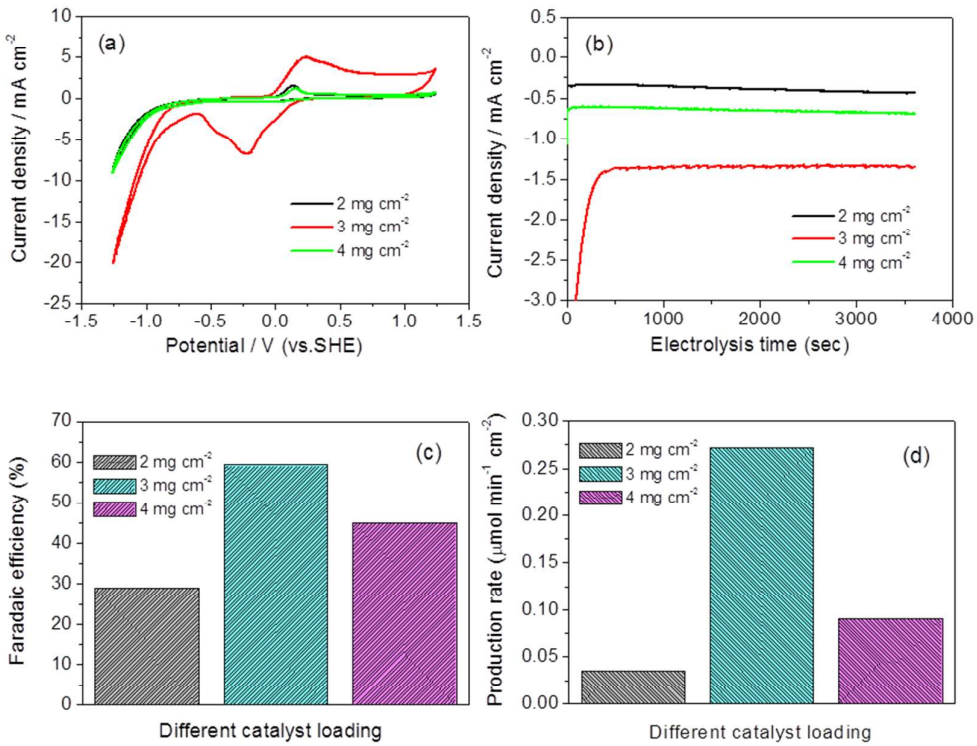

Fig. 9

1
2

Table 1 Physical characterization parameters of Cu_XO catalysts.

Catalysts	Morphology	Average size	BET surface area	Electrochemically active surface area
	-	(nm)	(m^2 g^{-1})	C (μF)
$Cu_XO_{180\text{-}2}$	Hierarchicl nanosphere	500	63.50	800
$Cu_XO_{180\text{-}15}$	Non-sphere	-	53.62	300
$Cu_XO_{220\text{-}2}$	Dense microshpere	2500	22.16	790

Table 2 Kinetic parameter, Faradaic efficiency and production rate of produced formate of CO_2 electroreduction.

Catalyst	Loading	Onset potential	Current density at potential = -1.25 V vs. SHE	Faradaic efficiency	Production rate
	(mg cm^{-2})	(V vs. SHE)	(mA cm^{-2})	(%)	(μmol min^{-1} cm^{-2})
$Cu_XO_{180\text{-}2}$	3	-0.55	-20.5	59.36	2.7×10^{-1}
$Cu_XO_{180\text{-}5}$	3	-0.80	-16.0	34.97	3.7×10^{-2}
$Cu_XO_{180\text{-}10}$	3	-0.85	-8.0	23.99	1.8×10^{-2}
$Cu_XO_{180\text{-}15}$	3	-0.85	-6.5	12.00	1.0×10^{-2}
$Cu_XO_{160\text{-}2}$	3	-0.85	-14.0	11.57	2.9×10^{-2}
$Cu_XO_{200\text{-}2}$	3	-0.90	-12.0	22.08	4.1×10^{-2}
$Cu_XO_{220\text{-}2}$	3	-0.60	-17.5	27.13	5.9×10^{-2}
$Cu_XO_{180\text{-}2}$	2	-0.85	-8.5	29.04	3.5×10^{-2}
$Cu_XO_{180\text{-}2}$	4	-0.85	-8.6	44.95	9.0×10^{-2}